Magnetic Weyl and quadratic nodal lines in inverse-Heusler-based fully compensated ferrimagnetic half-metals

Chengwu Xie,[1,*] Hongkuan Yuan,[1,*] Zeying Zhang,[2,†] and Xiaotian Wang[1,3,‡]

[1]*School of Physical Science and Technology, Southwest University, Chongqing 400715, China*

[2]*College of Mathematics and Physics, Beijing University of Chemical Technology, Beijing 100029, China*

[3]*Institute for Superconducting and Electronic Materials (ISEM), University of Wollongong, Wollongong 2500, Australia*

(Received 19 July 2022; accepted 29 August 2022; published 15 September 2022)

Heusler alloys, a class of easily prepared, highly ordered intermetallic compounds, were first reported in 1903. Since then, Heusler alloys have presented various physical phenomena in modern condensed-matter physics. Among Heusler alloys, Heusler-based fully compensated ferrimagnetic half-metals (FCF-HMs) are, particularly, relevant because they host fully spin polarization and have no net magnetic moment, making them have no stray field and less affected by external magnetic fields. Based on first-principles calculations and a tight-binding Hamiltonian model, we provide new insight into inverse-Heusler-based (IHB) FCF-HMs and reveal that they exhibit spin-polarized Weyl and quadratic nodal lines as well as spin-polarized drumheadlike surface states. This paper presents the electron-filling-based design rule and material candidates for IHB FCF-HMs and suggests that IHB FCF-HMs are promising candidates for follow-up investigations in the field of topological spintronics. Subsequent experimental confirmation of the topological states in IHB FCF-HMs is imminent.

DOI: 10.1103/PhysRevMaterials.6.094406

I. INTRODUCTION

Since Heusler [1] discovered the first Heusler alloy Cu_2MnSn in 1903, Heusler alloys have undergone different historical periods, presenting the majority of physical phenomena that pertain to modern condensed-matter physics, such as magnetic martensitic transformation [2,3], half-metallic behavior [4–7], superconductivity [8–12], thermoelectricity [13–16], heavy-fermion behavior [17,18], topological insulating behavior [19–27], spin-gapless semiconducting behavior [28–34], topological semimetallic behavior [35–40], perpendicular magnetic anisotropy [41–43], giant tunneling magnetoresistance [44,45], and magnetic skyrmions [46–48]. Heusler alloys have become vital material systems in many fields, particularly, in the past 40 yr.

To date, a series of Co_2-based full Heusler alloys [49–52] have been proposed as magnetic Weyl semimetals. For example, in 2016, Chang *et al.* [50] studied the topological magnetic states and Curie temperature of ferromagnetic Co_2TiX half-metal using first-principles calculations. They discovered that ferromagnetic Co_2TiX exhibits three topological nodal lines when spin-orbital coupling (SOC) is not added. In 2019, Belopolski *et al.* [51] examined the topology of a ferromagnetic Heusler alloy Co_2MnGa using photoemission spectroscopy and quantum transport. They observed sharp bulk Weyl fermion line dispersion and drumheadlike electronic wave functions on the alloy surface. In 2020, Li *et al.* [52] reported that the Co_2MnAl full Heusler alloy is a ferromagnetic Weyl semimetal that has a large room-temperature anomalous Hall effect and a tunable topology.

Shi *et al.* [53] claimed that the Ti_2MnAl alloy, which is a fully compensated ferrimagnetic semimetal with a *vanishing net* magnetic moment, has magnetic Weyl points with an opposite topological charge in contrast to the aforementioned Co-based ferromagnetic Heusler compounds with net magnetic moments. Subsequently, Noky *et al.* [54] predicted that the fully compensated ferrimagnets Ti_2MnX (X = Al, Ga, and In) exhibit a significant anomalous Nernst effect. Almost all studies on Heusler-based fully compensated ferrimagnets have concentrated only on nodal point states with zero-dimensional band crossings in momentum space, thus, far. *However, other studies have rarely investigated Heusler-based fully compensated ferrimagnets with nodal lines, i.e., one-dimensional band crossings in momentum space.*

In this paper, we used first-principles calculations and a tight-binding (TB) Hamiltonian model to investigate inverse-Heusler-based (IHB) fully compensated ferrimagnetic half-metals (FCF-HMs) [55–57] and study the rich magnetic nodal line states [58] in them. IHB FCF-HMs contain two types of magnetic nodal line states [58], i.e., a magnetic linear Weyl nodal line (WNL) and a magnetic quadratic nodal line (QNL). Fortunately, the two types of magnetic nodal lines in IHB FCF-HMs are symmetry dominated. That is, the magnetic WNL and QNL states must appear along the Γ-L and Γ-X high-symmetry paths, respectively. Herein, we present the electron-filling-based design rule for IHB FCF-HMs and propose a series of material candidates, such as -3%-strained Ti_2MnAl, -3%-strained Ti_2MnGa, Mn_3Al, Cr_2MnSb, and $+3\%$-strained Cr_2ZnSi collinear magnetic systems. The

*These authors contributed equally to this paper.

†Corresponding author. zzy@mail.buct.edu.cn

‡Corresponding author. xiaotianwang@swu.edu.cn

spin-polarized drumheadlike surface states related to the WNL and QNL in IHB FCF-HMs are also discussed in this paper.

II. COMPUTATIONAL METHODS

Theoretical calculations were performed using the density functional theory framework. The generalized gradient approximation [59] with Perdew-Burke-Ernzerhof formalism was used for the exchange-correlation energy, and the projector augmented-wave method [60] was used for interactions between the ions and the valence electrons. Moreover, a cutoff energy of 500 eV was chosen for the plane-wave set, and a Γ-centered k grid of 15 × 15 × 15 was sampled for the Brillouin zone (BZ). The lattice constants and atomic positions of the Heusler alloys in our paper were fully relaxed with a convergence criterion of 10^{-6} eV for the self-consistent field procedure and a maximum residual force per atom of less than −0.001 eV/Å. The surface states were calculated using the WANNIERTOOLS software [61] based on the maximally localized Wannier functions [62]. The TB Hamiltonian model was obtained using the MAGNETICTB code [63], which can generate the TB model for any arbitrary magnetic space group.

III. DESIGN RULE FOR IHB FCF-HMS

In this section, we would like to explain the difference between Heusler-based FCF-HMs and Heusler-based ferromagnetic HMs. Heusler-based ferromagnetic HMs [64] are spintronic materials with 100% spin polarization around the Fermi level. Heusler-based ferromagnetic HMs usually have an energy gap in one spin direction and a metallic state in the other spin direction. They should have an integer net spin moment in Bohr magnetons per unit cell because of the quantization of the valence electrons. Figure 1(a) depicts the schematic of Heusler-based ferromagnetic HMs. The number of spin-up valence electrons ($N_V\uparrow$) is not equal to that of spin-down valence electrons ($N_V\downarrow$). Figure 1(b) depicts the schematic of Heusler-based FCF-HMs. The half-metallic gap is still maintained. However, $N_V\uparrow = N_V\downarrow$, resulting in 100% spin polarization and a vanishing net magnetic moment (i.e., a zero-net magnetic moment). Heusler-based FCF-HMs are insensitive to external magnetic fields and produce no stray fields, providing them with an added advantage for practical applications.

As shown in Figs. 2(a) and 2(b), inverse-Heusler alloys [65–67] with the formula X_2YZ (X and Y are transition-metal atoms, and Z is a sp element) have a structure that contains four interpenetrating face-centered cubic lattices with the X, X, Y, and Z atoms occupying the (0, 0, 0), (0.25, 0.25, 0.25), (0.5, 0.5, 0.5), and (0.75, 0.75, 0.75) Wyckoff coordinates, respectively.

Here, we present the electron-filling-based design rule for IHB FCF-HMs to narrow down their search range. There are some typical cases of half-metallic gaps around the Fermi level for the inverse-Heusler alloys. In particular, there may be 9, 12, or 14 $N_V\uparrow$ ($N_V\downarrow$) below the gap in both spin directions. However, since $N_V\uparrow = N_V\downarrow$ for the FCF-HMs, band gaps near the Fermi level can be obtained in both spin directions

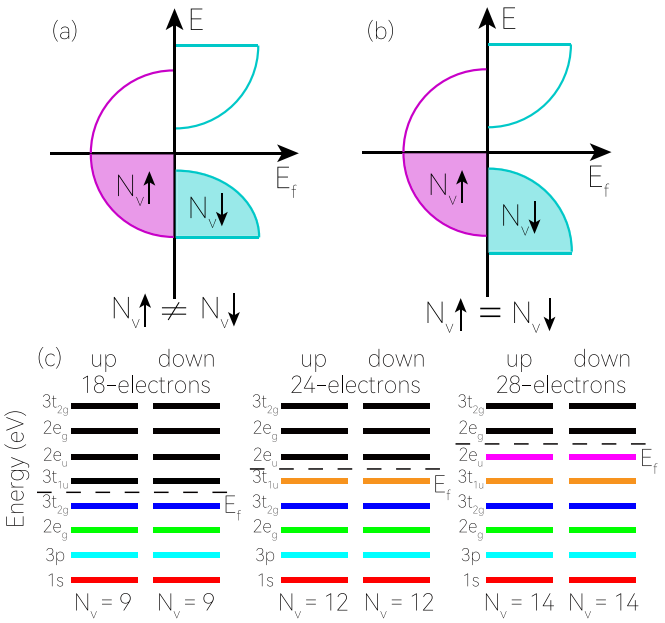

FIG. 1. (a) and (b) Schematics of Heusler-based ferromagnetic HMs and FCF-HMs, respectively. (c) Schematic of the energy levels of the band structures for both spin directions for the 18, 24, and 28 valence electron FCF-HMs with an inverse-Heusler structure.

by having $N_V\uparrow - N_V\downarrow$ fillings of 9-9, 12-12, and 14-14 in both spin directions [see Fig. 1(c)]. Therefore, inverse-Heusler alloys with 18, 24, and 28 N_V are suitable candidates for predicting IHB FCF-HMs.

IV. MATERIAL CANDIDATES FOR IHB FCF-HMS

We selected a series of inverse-Heusler alloys (see Table I) with 18, 24, or 28 N_V based on the above-mentioned design rule for IHB FCF-HMs in order to examine their FCF-HM behaviors. It should be noted that Mn_3Z (Z = B, Al, Ga, In, and Tl) can be viewed as a special X_2XZ inverse-Heusler alloy if X is considered to be equal to Y. Figures S1–S7 in the Supplemental Material (SM) [68] display the calculated band structures of the selected inverse-Heusler alloys, and Table I also lists their calculated magnetic moments and physics natures. Figures S1–S7 in the SM [68] and Table I present three FCF-SGSs, four FCF magnetic semiconductors, six FCF-HMs, eight FCF metals, and 18 ferrimagnetic metals (FIM-metals).

The five IHB FCF-HMs are −3%-strained Ti_2MnAl, −3%-strained Ti_2MnGa, Mn_3Al, Cr_2MnSb, and +3%-strained Cr_2ZnSi (see Table S1 in the SM [68]). As examples, the band structures of the −3%-strained Ti_2MnAl, Mn_3Al, and +3%-strained Cr_2ZnSi alloys are presented in Figs. 3(a)–3(c), respectively. The first two alloys have spin-up bands that overlap with the Fermi level, but the spin-down bands do not. In contrast, +3%-strained Cr_2ZnSi has a half-metallic gap in the spin-up direction and a metallic state in the spin-down direction. As shown in Fig. 3, the d orbitals of the Mn, Ti, or Cr transition-metal atoms contribute to the bands near the Fermi level. As shown in Figs. 3(a)–3(c), there are $N_V\uparrow - N_V\downarrow$ fillings of 9-9, 12-12, and 14-14 in both

TABLE I. Obtained lattice constants, N_V, M_t, and physical natures for a series of inverse-Heusler compounds.

Materials	$a = b = c$ (Å)	N_V	M_t	Physical nature
Ti_2MnB	5.7352	18	0	FCF-MS
Ti_2MnAl	6.2449	18	0	FCF-spin-gapless semiconductors (-SGS)
Ti_2MnAl (−3%)	6.0576	18	0	FCF-HM
Ti_2MnGa	6.2151	18	0	FCF-SGS
Ti_2MnGa (−3%)	6.0286	18	0	FCF-HM
Ti_2MnIn	6.4852	18	0	FCF-MS
Ti_2MnTl	6.5279	18	0	FCF-MS
Ti_2VN	5.8419	18	0.635	FIM-metal
Ti_2VP	6.0719	18	0.006	FCF-metal
Ti_2VAs	6.2261	18	0.015	FIM-metal
Ti_2VSb	6.482	18	0	FCF-MS
Ti_2VBi	6.6171	18	0.009	FCF-metal
Mn_3B	5.3989	24	0.086	FIM-metal
Mn_3Al	5.80	24	0	FCF-HM
Mn_3Ga	5.829	24	0.14	FIM-metal
Mn_3In	6.2853	24	2.476	FIM-metal
Mn_3Tl	6.4085	24	3.317	FIM-metal
Mn_2CrC	5.3901	24	0.442	FIM-metal
Mn_2CrSi	5.7302	24	0.017	FIM-metal
Mn_2CrGe	5.8449	24	0.026	FIM-metal
Mn_2CrSn	6.1355	24	0.002	FCF-metal
Mn_2CrPb	6.2599	24	0.023	FIM-metal
Cr_2CoB	5.3979	24	0	FCF-metal
Cr_2CoAl	5.7973	24	0.02	FIM-metal
Cr_2CoGa	5.8236	24	0.083	FIM-metal
Cr_2CoIn	6.1346	24	0.161	FIM-metal
Cr_2CoTl	6.2227	24	0.268	FIM-metal
Cr_2MnN	5.4302	24	0.006	FCF-metal
Cr_2MnP	5.6088	24	0.106	FIM-metal
Cr_2MnAs	5.787	24	0.011	FIM-metal
Cr_2MnSb	6.0658	24	0.001	FCF-HM
Cr_2MnBi	6.2424	24	0.008	FCF-metal
Cr_2ZnC	5.657	28	0.164	FIM-metal
Cr_2ZnSi	5.8516	28	0	FCF-SGS
Cr_2ZnSi (+3%)	6.0271	28	0	FCF-HM
Cr_2ZnGe	6.0353	28	0.001	FCF-metal
Cr_2ZnSn	6.1355	28	0.002	FCF-metal
Cr_2ZnPb	6.6238	28	0.156	FIM-metal

spin directions for the −3%-strained Ti_2MnAl, Mn_3Al, and +3%-strained Cr_2ZnSi alloys, respectively. These three IHB FCF-HMs obey the Slater-Pauling rule that $M_t = N_V - 18$, $M_t = N_V - 24$, and $M_t = N_V - 28$ (where M_t denotes the total magnetic moment) [85,86]. Hence, IHB FCF-HMs must obey the above-mentioned electron-filling rule and the Slater-Pauling rule [see Fig. 1(c)] both of which can be used to narrow down their search range in follow-up studies.

V. RICH MAGNETIC NODAL LINE STATES IN IHB FCF-HMS

A. Example: The Mn_3Al compound

To further prove the coexistence of magnetic WNL and QNL states in IHB FCF-HMs with space-group (SG) No. 216, we selected Mn_3Al as an example and examined its band structure and corresponding magnetic nodal line signatures. It is worth noting that Jamer *et al.* [87] confirmed the FCF-HM behavior of the Mn_3Al bulk via first-principles calculations in 2017. They [87] also synthesized 50-nm Mn_3Al thin films using the molecular beam epitaxy and annealed them at various temperatures and confirmed that the thin films possessed nominal zero moments based on the polarized-neutron reflectometry data. The coexistence of the magnetic WNL and QNL states in the −3%-strained Ti_2MnAl, −3%-strained Ti_2MnGa, Cr_2MnSb, and +3%-strained Cr_2ZnSi IHB FCF-HMs are also exhibited in Fig. S8 (see the SM in Ref. [68]).

Since Mn_3Al has a semiconducting gap in the spin-down direction, we only focused on the topological states around the Fermi level in the spin-up direction. Figure 4(a) depicts the spin-up band structure of Mn_3Al along the Γ-X-$U(K)$-Γ-L-W-X paths. The magnetic QNL and WNL appear along the Γ-X and Γ-L paths, respectively. We display the dispersion for generic points on the lines along the Γ-X

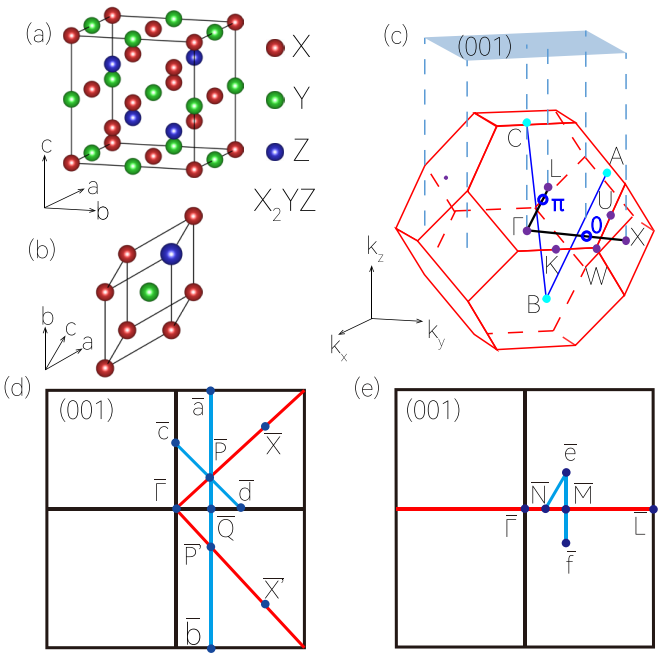

FIG. 2. (a) and (b) Unit and primitive cells for the inverse-Heusler compound X_2YZ, respectively. (c) Three-dimensional BZ and some selected symmetry paths. The QNL and WNL along Γ-X the Γ-L and paths have 0 and π Berry phase values, respectively. (d) and (e) Schematics of the projection of the QNL and WNL states onto the (001) surface, respectively, as well as some selected surface paths on the (001) surface.

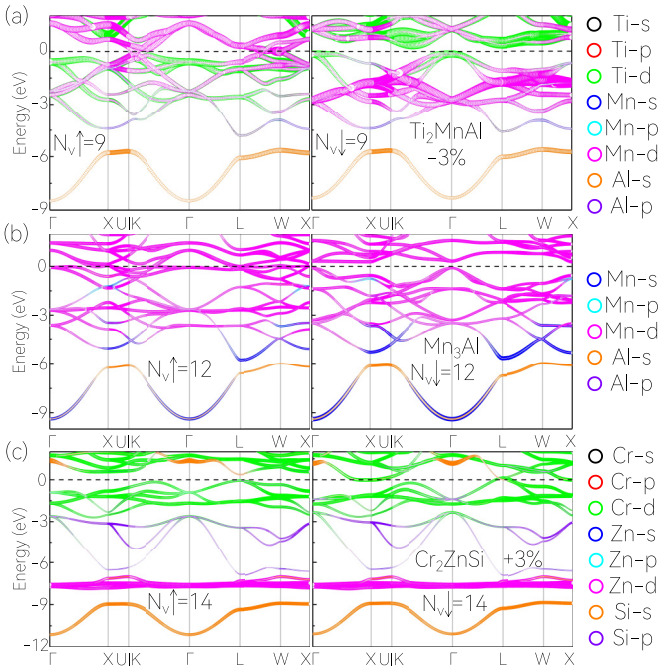

FIG. 3. Orbital-resolved band structures for the (a) −3%-strained Ti_2MnAl, (b) Mn_3Al, and (c) +3%-strained Cr_2ZnSi alloys. $N_V\uparrow$ and $N_V\downarrow$ are also exhibited.

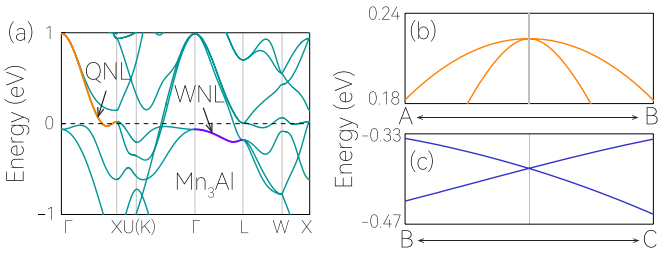

FIG. 4. (a) Spin-up band structure of Mn_3Al. Band structures of the Mn_3Al compound along the (b) A-B and (c) B-C paths.

and Γ-L paths to confirm the order of energy dispersions of the nodal lines. Figures 4(b) and 4(c) depict the spin-up band structures of Mn_3Al along the A-B and B-C paths [see the paths in Fig. 2(b)]. The generic points on the lines along the Γ- L and Γ-X paths exhibit a linear order dispersion [see Fig. 4(c)] and a quadratic order dispersion [see Fig. 4(b)], respectively.

The following should be noted: (i) The WNL along the Γ-L path is nontrivial, whereas the QNL along the Γ-X path is trivial. To examine whether the WNL and QNL are nontrivial or not, we calculated the Berry phase for the WNL and QNL, which is defined as $\gamma = \oint_{\mathcal{C}} A(\mathbf{k}) \cdot d\mathbf{k}$, where $A(\mathbf{k})$ is the Berry connection, and $\mathcal{C}$ is a closed path surrounding the lines in the momentum space. As shown in Fig. 2(c), the WNL along the Γ-L path has a π-Berry phase value, indicating that it is topologically nontrivial [88–90]. However, the QNL along the Γ-X path has a 0 Berry phase value, indicating that it is trivial. (ii) It is well known that the SOC effect will induce a gap for the nodal line states [91]. Figure S9 (see the SM [68]) depicts the band structure of Mn_3Al under SOC along the Γ-X-U(K)-Γ-L-W-X paths. The WNL is opened by SOC with a gap of less than 6.8 meV (see region B), and the QNL is opened by SOC with a gap of less than 26 meV (see region A). The values of the SOC-induced gaps for the WNL and QNL are less than the energy scale of room temperature (26 meV). Table S2 (see the SM [68]) shows that the values of the SOC-induced gaps for the WNL and QNL are smaller than those of a few well-known topological nodal line materials (with SOC-induced gaps larger than 30 meV).

B. Lattice model with SG 216

If SOC is not considered, the spin and orbital degrees of freedom are independent and can, therefore, be viewed as different subspaces. The spin-up and spin-down channels are decoupled with a chosen spin-polarization axis, making it possible to view the bands for each spin direction as a spinless system. A spinless lattice model is presented herein to demonstrate the existence of WNL and QNL states in materials with SG 216. A unit cell with one site (0,0,0) was considered in this spinless lattice model, and d_{xy}, d_{xz}, d_{yz}, $d_{x^2-y^2}$, and d_{z^2} orbitals were placed on this site. The five-band TB Hamiltonian with only considering up to nearest-neighbor hopping can be written as (see the SM [68] for a detailed Hamiltonian in momentum space),

$$H = \sum_{\langle ij\rangle\alpha\beta} t_{ij}^{\alpha\beta} c_{i\alpha}^{\dagger} c_{j\beta} + \text{H.c.} \quad (1)$$

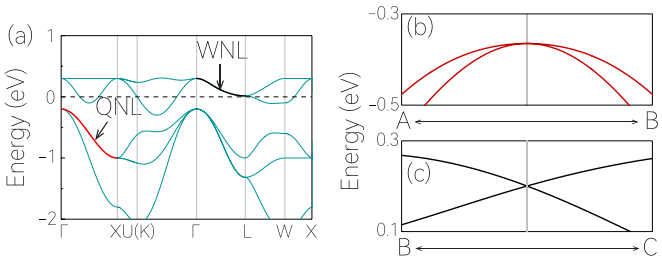

FIG. 5. (a) Band structure of the spinless lattice model with SG 216. Band structures of spinless lattice models along the (b) A-B and (c) B-C paths.

Figure 5(a) depicts the band structure of the spinless lattice model [Eq. (1)]; $e = -1$, $r = 0.1$, $t_1 = 0.1$, $t_2 = 0.1$, and $t_3 = 0.1$ for the bands along the Γ-X-U(K)-Γ-L-W-X paths. There are WNL (the black line) and QNL (the red line) along the Γ-L and Γ-X paths, respectively. As shown in Figs. 5(b) and 5(c), the generic points on the lines along the Γ-L and Γ-X paths exhibit a linear order dispersion [see Fig. 5(c)] and a quadratic order dispersion [see Fig. 5(b)], respectively. The results of the nodal line state in the spinless lattice model with SG 216 agree well with those in the spin-up direction of Mn_3Al.

C. Symmetry-enforced of QNLs and WNLs

Next, we used symmetry analysis to analyze the appearance of WNL and QNL in material candidates with SG 216. Since the spin-up and spin-down bands have no symmetry connecting them, they can be considered separately when SOC is neglected. When the two-dimensional corepresentation along the Γ-X path of SG 216 (i.e., $\Delta_2\Delta_4$) is considered, the matrix representations for $\Delta_2\Delta_4$ can be easily obtained using space-group *Irep* [92],

$$\delta_{dc} = \delta_3, \qquad C_{2z}\mathcal{K} = -\delta_1. \tag{2}$$

It is noticeable that the system has no time-reversal symmetry, but the complex conjugate operator $\mathcal{K}$ for each spin channel is reserved. Thus, the effective Hamiltonian constrained by δ_{dc} and $C_{2z}\mathcal{K}$ around an arbitrary point on Γ-X can be written as

$$\begin{aligned} H = {} & \varepsilon + c_1 k_y + c_2\left(k_x^2 + k_z^2\right) + c_3 k_y^2 \\ & + c_4 k_x k_y \delta_3 (c_5\delta_1 + c_6\delta_2)\left(k_x^2 - k_z^2\right), \end{aligned} \tag{3}$$

which confirms that there are degenerate bands along Γ-X. Since the leading-order dispersion in the band splitting is quadratic, the nodal line along the Γ-X path belongs to the QNL [93–95].

Similarly, when the two-dimensional corepresentation along Γ-L (i.e., Λ_3) is considered, the matrix representations and the effective Hamiltonian for Λ_3 can be written as

$$C_{31}^{+} = e^{-(2i\pi/3)\delta_2}, \qquad \delta_{db} = \delta_3, \tag{4}$$

Thus, the effective Hamiltonian constrained by δ_{db} and C_{31}^{+} around any arbitrary point on Γ-L can be written as

$$\begin{aligned} H = {} & \varepsilon + c_1(k_x + k_y + k_z) \\ & + \sqrt{3}c_2(k_x - k_y)\delta_1 c_2(k_x + k_y - 2k_z)\delta_3. \end{aligned} \tag{5}$$

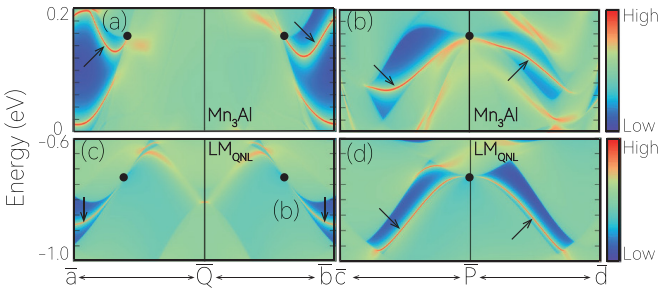

FIG. 6. The (001) surface states in Mn_3Al along the (a) $\bar{a}$-$\bar{Q}$-$\bar{b}$ and (b) $\bar{c}$-$\bar{P}$-$\bar{d}$ surface paths. Surface states in the lattice model (LM) with SG 216 along the (c) $\bar{a}$-$\bar{Q}$-$\bar{b}$ and (d) $\bar{c}$-$\bar{P}$-$\bar{d}$ surface paths. The two projection points of the QNL are indicated as $\bar{P}$ and $\bar{P}'$ (highlighted by black balls). The drumheadlike surface states are marked by black arrows.

This confirms that the degenerate bands of Γ-L belong to the WNL [96,97].

VI. SPIN-POLARIZED DRUMHEADLIKE SURFACE STATES IN IHB FCF-HMS

In this section, we discuss the surface states corresponding to the WNL and QNL states in Mn_3Al and the lattice model with SG 216. Figure 2(d) displays the projection of the QNL onto the (001) surface in materials with SG 216. Figure 6 depicts the projected surface states along the $\bar{a}$-$\bar{Q}$-$\bar{b}$ and $\bar{c}$-$\bar{P}$-$\bar{d}$ surface paths on the (001) surface shown in Fig. 2(d). The two projection points of the QNL are $\bar{P}$ and $\bar{P}'$. Figures 6(a) and 6(b) depict the surface states in the realistic Mn_3Al compound, and Figs. 6(c) and 6(d) depict the surface states in the lattice model with SG. 216. As shown in Fig. 6, there are drumheadlike surface bands that originate from $\bar{P}$ and $\bar{P}'$. Note that the drumheadlike surface states in Mn_3Al are spin polarized [98–101] because the bulk of Mn_3Al has 100% spin polarization.

Moreover, Fig. 2(e) displays the projection of the WNL onto the (001) surface in a compound with SG 216. Figure 7 displays the projected surface states along the $\bar{e}$-$\bar{M}$-$\bar{f}$ and $\bar{M}$-$\bar{e}$-$\bar{N}$ surface paths on the (001) surface shown in Fig. 2(e).

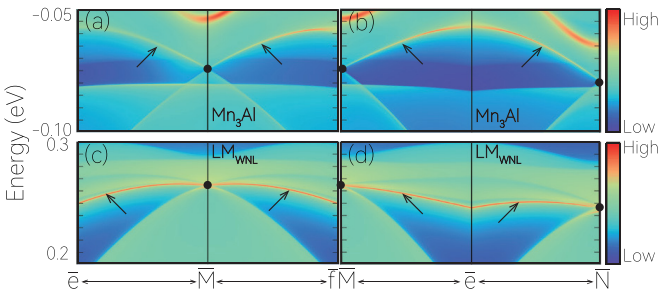

FIG. 7. The (001) surface states in Mn_3Al along the (a) $\bar{e}$-$\bar{M}$-$\bar{f}$ and (b) $\bar{M}$-$\bar{e}$-$\bar{N}$ surface paths. Surface states in the lattice model with SG 216 along the (c) $\bar{e}$-$\bar{M}$-$\bar{f}$ and (d) $\bar{M}$-$\bar{e}$-$\bar{N}$ surface paths. The two projection points of the WNL are denoted as $\bar{M}$ and $\bar{N}$ (highlighted by black balls). The drumheadlike surface states are marked by black arrows.

The two projection points of the WNL are denoted as $\bar{M}$ and $\bar{N}$. Figures 7(a)–7(d) depict the surface states in Mn_3Al and the lattice model with SG 216 along the $\bar{e}$-$\bar{M}$-$\bar{f}$ and $\bar{M}$-$\bar{e}$-$\bar{N}$ paths, respectively. As shown in Fig. 7, there are drumheadlike surface states that connect the projected band crossings $\bar{M}$ and $\bar{N}$.

VII. CONCLUSIONS AND REMARKS

We provide a new horizon for studying IHB FCF-HMs using first-principles calculations and a TB Hamiltonian model, and we demonstrate that they exhibit spin-polarized Weyl and quadratic nodal lines and spin-polarized drumheadlike surface states. This paper also presents the design rule and material candidates for IHB FCF-HMs.

Furthermore, it is worth noting that: (1) although Heusler-based FCF-HMs have been reported in some previous studies [55–57], it was reported Heusler-based FCF-HMs as potential candidates with magnetic QNL states here. (2) Magnetic QNLs have only recently been reported theoretically [58] and the proposed candidates with QNL may be challenging to synthesize experimentally. Hence, it is necessary to search for an easily prepared class of materials with vanishing net magnetic moments, 100% spin polarization, and magnetic WNL and QNL. This paper demonstrates that collinear magnetic systems—IHB FCF-HMs with zero net magnetic moments—have rich magnetic nodal line states. Our paper is valuable for comprehensively understanding the one-dimensional topological signature (i.e., the magnetic nodal line state) in zero-moment magnetic materials. (3) Since the magnetic WNL and QNL states in IHB FCF-HMs are symmetry dominated, they must appear along the Γ-L and Γ-X paths. Although symmetry requires the occurrence of magnetic WNL and QNL states in IHB FCF-HMs, it does not limit the energies of these two nodal line states. (4) In most cases, the nodal lines suffer sizable SOC-induced gaps. Therefore, one may have to focus on material candidates with light elements to reduce the value of SOC-induced gaps in the magnetic WNL and QNL states in IHB FCF-HMs. (5) The search for IHB FCF-HMs with excellent magnetic nodal line states (i.e., near the Fermi level and nearly immune from SOC) remains an important research topic for follow-up investigations. (6) Some titanium-based full-Heusler alloys, such as Ti_2MnAl and Ti_2MnGa, are more stable in regular (i.e.,, $L2_1$-type) Heusler structure than inverse Heusler structure [102–104]. Note that full-Heusler alloys may show abruptly different spintronic properties, depending on their regular or inverse Heusler structures. For example, Ti_2MnAl with an inverse Heusler structure is a FCF-SGS [105,106], however, Ti_2MnAl with regular Heusler structure is a plain paramagnetic metal [102].

ACKNOWLEDGMENTS

Z.Z. is grateful for support from the National Natural Science Foundation of China (Grant No. 12004028). X.W. is grateful for the support from the National Natural Science Foundation of China (Grant No. 51801163). H.Y. is grateful for the support from the the National Natural Science Foundation of China (Grants No. 11874306 and No. 12174320) and the Natural Science Foundation of Chongqing (Grants No. cstc2021jcyj-msxmX0209 and No. cstc2022ycjh-bgzxm0127).

[1] F. Heusler, Verh. Dtsch. Phys. Ges. **5**, 219 (1903).
[2] G.-H. Yu, Y.-L. Xu, Z.-H. Liu, H.-M. Qiu, Z.-Y. Zhu, X.-P. Huang, and L.-Q. Pan, Rare Met. **34**, 527 (2015).
[3] W. H. Wang, J. L. Chen, Z. H. Liu, G. H. Wu, and W. S. Zhan, Phys. Rev. B **65**, 012416 (2001).
[4] I. Galanakis, Phys. Rev. B **71**, 012413 (2005).
[5] S. Roy, N. Khan, R. Singha, A. Pariari, and P. Mandal, Phys. Rev. B **99**, 214414 (2019).
[6] V. Alijani, J. Winterlik, G. H. Fecher, S. S. Naghavi, and C. Felser, Phys. Rev. B **83**, 184428 (2011).
[7] R. A. de Groot, F. M. Mueller, P. G. van Engen, and K. H. J. Buschow, Phys. Rev. Lett. **50**, 2024 (1983).
[8] T. Klimczuk, C. H. Wang, K. Gofryk, F. Ronning, J. Winterlik, G. H. Fecher, J.-C. Griveau, E. Colineau, C. Felser, J. D. Thompson, D. J. Safarik, and R. J. Cava, Phys. Rev. B **85**, 174505 (2012).
[9] J. Winterlik, G. H. Fecher, A. Thomas, and C. Felser, Phys. Rev. B **79**, 064508 (2009).
[10] H. Xiao, T. Hu, W. Liu, Y. L. Zhu, P. G. Li, G. Mu, J. Su, K. Li, and Z. Q. Mao, Phys. Rev. B **97**, 224511 (2018).
[11] J. Winterlik, G. H. Fecher, C. Felser, M. Jourdan, K. Grube, F. Hardy, H. von Löhneysen, K. L. Holman, and R. J. Cava, Phys. Rev. B **78**, 184506 (2008).
[12] Q.-Z. Wang, J. Yu, and C.-X. Liu, Phys. Rev. B **97**, 224507 (2018).
[13] T. J. Zhu, C. G. Fu, H. H. Xie, Y. T. Liu, and X. B. Zhao, Adv. Energy Mater. **5**, 1500588 (2015).
[14] B. Hinterleitner, I. Knapp, M. Poneder, Y. Shi, H. Müller, G. Eguchi, C. Eisenmenger-Sittner, M. Stöger-Pollach, Y. Kakefuda, and N. Kawamoto *et al.*, Nature (London) **576**, 85 (2019).
[15] C. Fu, S. Bai, Y. Liu, Y. Tang, L. Chen, X. Zhao, and T. Zhu, Nat. Commun. **6**, 8144 (2015).
[16] K. Xia, C. Hu, C. Fu, X. Zhao, and T. Zhu, Appl. Phys. Lett. **118**, 140503 (2021).
[17] Z. Liu, L. Yang, S-C. Wu, C. Shekhar, J. Jiang, H. Yang, Y. Zhang, S-K. Mo, Z. Hussain, B. Yan, C. Felser, and Y. Chen, Nat. Commun. **7**, 12924 (2016).
[18] C. S. Lue, J. H. Ross, Jr., C. F. Chang, and H. D. Yang, Phys. Rev. B **60**, R13941 (1999).
[19] B. Yan and A. de Visser, MRS Bull. **39**, 859 (2014).
[20] W. Al-Sawai, H. Lin, R. S. Markiewicz, L. A. Wray, Y. Xia, S. Y. Xu, M. Z. Hasan, and A. Bansil, Phys. Rev. B **82**, 125208 (2010).
[21] D. Xiao, Y. Yao, W. Feng, J. Wen, W. Zhu, X. Q. Chen, G. M. Stocks, and Z. Zhang, Phys. Rev. Lett. **105**, 096404 (2010).

[22] S. Chadov, X. Qi, J. Kübler, G. H. Fecher, C. Felser, and S. C. Zhang, Nature Mater. **9**, 541 (2010).

[23] H. Lin, L. A. Wray, Y. Xia, S. Xu, S. Jia, R. J. Cava, A. Bansil, and M. Z. Hasan, Nature Mater. **9**, 546 (2010).

[24] S.-Y. Lin, M. Chen, X.-B. Yang, Y.-J. Zhao, S.-C. Wu, C. Felser, and B. Yan, Phys. Rev. B **91**, 094107 (2015).

[25] W. Wang, Y. Du, G. Xu, X. Zhang, E. Liu, Z. Liu, Y. Shi, J. Chen, G. Wu, and X. Zhang, Sci. Rep. **3**, 2181 (2013).

[26] G. Xu, W. Wang, X. Zhang, Y. Du, E. Liu, S. Wang, G. Wu, Z. Liu, and X. X. Zhang, Sci. Rep. **4**, 5709 (2015).

[27] Z. Hou, Y. Wang, E. Liu, H. Zhang, W. Wang, and G. Wu, Appl. Phys. Lett. **107**, 202103 (2015).

[28] X. Wang, Z. Cheng, J. Wang, X. L. Wang, and G. Liu, J. Mater. Chem. C **4**, 7176 (2016).

[29] L. Bainsla, A. I. Mallick, M. M. Raja, A. K. Nigam, B. S. D. C. S. Varaprasad, Y. K. Takahashi, A. Alam, K. G. Suresh, and K. Hono, Phys. Rev. B **91**, 104408 (2015).

[30] S. Ouardi, G. H. Fecher, C. Felser, and J. Kübler, Phys. Rev. Lett. **110**, 100401 (2013).

[31] L. Bainsla, A. I. Mallick, M. M. Raja, A. A. Coelho, A. K. Nigam, D. D. Johnson, A. Alam, and K. G. Suresh, Phys. Rev. B **92**, 045201 (2015).

[32] Q. Gao, I. Opahle, and H. Zhang, Phys. Rev. Mater. **3**, 024410 (2019).

[33] A. Jakobsson, P. Mavropoulos, E. Şaşıoğlu, S. Blügel, M. Ležaič, B. Sanyal, and I. Galanakis, Phys. Rev. B **91**, 174439 (2015).

[34] J. Wang, H. Yuan, Y. Liu, X. Wang, and G. Zhang, Phys. Rev. B **106**, L060407 (2022).

[35] C. Mondal, C. K. Barman, B. Pathak, and A. Alam, Phys. Rev. B **100**, 245151 (2019).

[36] P.-J. Guo, H.-C. Yang, K. Liu, and Z.-Y. Lu, Phys. Rev. B **95**, 155112 (2017).

[37] G. Chang, S.-Y. Xu, X. Zhou, S.-M. Huang, B. Singh, B. Wang, I. Belopolski, J. Yin, S. Zhang, and A. Bansil *et al.*, Phys. Rev. Lett. **119**, 156401 (2017).

[38] Z. Wang, M. G. Vergniory, S. Kushwaha, M. Hirschberger, E. V. Chulkov, A. Ernst, N. P. Ong, R. J. Cava, and B. A. Bernevig, Phys. Rev. Lett. **117**, 236401 (2016).

[39] C. K. Barman, C. Mondal, B. Pathak, and A. Alam, Phys. Rev. B **99**, 045144 (2019).

[40] H.-S. Jin, Y.-J. Song, W. E. Pickett, and K.-W. Lee, Phys. Rev. Mater. **3**, 021201(R) (2019).

[41] S. V. Faleev, Y. Ferrante, J. Jeong, M. G. Samant, B. Jones, and S. S. P. Parkin, Phys. Rev. Mater. **1**, 024402 (2017).

[42] M. S. Gabor, M. Nasui, and A. Timar-Gabor, Phys. Rev. B **100**, 144438 (2019).

[43] T. L. Brown-Heft, J. A. Logan, A. P. McFadden, C. Guillemard, P. Le Fèvre, F. Bertran, S. Andrieu, and C. J. Palmstrøm, Phys. Rev. Mater. **2**, 034402 (2018).

[44] W. H. Wang, H. Sukegawa, and K. Inomata, Phys. Rev. B **82**, 092402 (2010).

[45] W. Wang, E. Liu, M. Kodzuka, H. Sukegawa, M. Wojcik, E. Jedryka, G. H. Wu, K. Inomata, S. Mitani, and K. Hono, Phys. Rev. B **81**, 140402(R) (2010).

[46] R. Saha, A. K. Srivastava, T. Ma, J. Jena, P. Werner, V. Kumar, C. Felser, and S. S. P. Parkin, Nat. Commun. **10**, 5305 (2019).

[47] W. Akhtar, A. Hrabec, S. Chouaieb, A. Haykal, I. Gross, M. Belmeguenai, M. S. Gabor, B. Shields, P. Maletinsky, A. Thiaville, S. Rohart, and V. Jacques, Phys. Rev. Appl. **11**, 034066 (2019).

[48] A. K. Nayak, V. Kumar, T. Ma, P. Werner, E. Pippel, R. Sahoo, F. Damay, U. K. Rößler, C. Felser, and S. S. P. Parkin, Nature (London) **548**, 561 (2017).

[49] K. Manna, Y. Sun, L. Muechler, J. Kübler, and C. Felser, Nat. Rev. Mater. **3**, 244 (2018).

[50] G. Chang, S.-Y. Xu, H. Zheng, B. Singh, C.-H. Hsu, I. Belopolski, D. S. Sanchez, G. Bian, N. Alidoust, H. Lin, and M. Z. Hasan, Sci. Rep. **6**, 38839 (2016).

[51] I. Belopolski, K. Manna, D. S. Sanchez, G. Chang, B. Ernst, J. Yin, S. S. Zhang, T. Cochran, N. Shumiya, H. Zheng, B. Singh, G. Bian, D. Multer, M. Litskevich, X. Zhou, S. M. Huang, B. Wang, T. R. Chang, S. Y. Xu, and A. Bansil *et al.*, Science **365**, 1278 (2019).

[52] P. Li, J. Koo, W. Ning, J. Li, L. Miao, L. Min, Y. Zhu, Y. Wang, N. Alem, C.-X. Liu, Z. Mao, and B. Yan, Nat. Commun. **11**, 3476 (2020).

[53] W. Shi, L. Muechler, K. Manna, Y. Zhang, K. Koepernik, R. Car, J. van den Brink, C. Felser, and Y. Sun, Phys. Rev. B **97**, 060406(R) (2018).

[54] J. Noky, J. Gayles, C. Felser, and Y. Sun, Phys. Rev. B **97**, 220405(R) (2018).

[55] I. Galanakis, K. Ozdogan, E. Sasioglu, and B. Aktas, Phys. Rev. B **75**, 172405 (2007).

[56] M. Žic, K. Rode, N. Thiyagarajah, Y. C. Lau, D. Betto, J. M. D. Coey, S. Sanvito, K. J. O'Shea, C. A. Ferguson, D. A. MacLaren, and T. Archer, Phys. Rev. B **93**, 140202(R) (2016).

[57] I. Galanakis and E. Şaşıoğlu, Appl. Phys. Lett. **99**, 052509 (2011).

[58] Z. Zhang, Z. M. Yu, and S. A. Yang, Phys. Rev. B **103**, 115112 (2021).

[59] J. P. Perdew, K. Burke, and M. Ernzerhof, Phys. Rev. Lett. **77**, 3865 (1996).

[60] P. E. Blöchl, Phys. Rev. B **50**, 17953 (1994).

[61] Q. S. Wu, S. N. Zhang, H.-F. Song, M. Troyer, and A. A. Soluyanov, Comput. Phys. Commun. **224**, 405 (2018).

[62] A. A. Mostofi, J. R. Yates, Y.-S. Lee, I. Souza, D. Vanderbilt, and N. Marzari, Comput. Phys. Commun. **178**, 685 (2008).

[63] Z. Zhang, Z.-M. Yu, G.-B. Liu, and Y. Yao, Comput. Phys. Commun. **270**, 108153 (2022).

[64] I. Galanakis and Ph. Mavropoulos, J. Phys.: Condens. Matter **19**, 315213 (2007).

[65] S. Skaftouros, K. özdožan, E. Şaşıoğlu, and I. Galanakis, Appl. Phys. Lett. **102**, 022402 (2013).

[66] Y. Venkateswara, S. S. Samatham, A. K. Patel, P. D. Babu, M. R. Varma, K. G. Suresh, and A. Alam, Phys. Rev. B **104**, 094402 (2021).

[67] J. Ma, J. He, D. Mazumdar, K. Munira, S. Keshavarz, T. Lovorn, C. Wolverton, A. W. Ghosh, and W. H. Butler, Phys. Rev. B **98**, 094410 (2018).

[68] See Supplemental Material at http://link.aps.org/supplemental/10.1103/PhysRevMaterials.6.094406 for the detailed Hamiltonian in momentum space, the spin-polarized band structures for a series of inverse-Heusler compounds, some proposed FCF-HMs among inverse-Heusler compounds, the related Slater-Pauling rules, selected well-known nodal line materials, their SOC-induced gaps, and band structure of Mn_3Al with SOC, which includes Refs. [69–84].

[69] X. Zhang, Z.-M. Yu, X.-L. Sheng, H. Y. Yang, and S. A. Yang, Phys. Rev. B **95**, 235116 (2017).

[70] L. Jin, X. M. Zhang, X. F. Dai, L. Y. Wang, H. Y. Liu, and G. D. Liu, IUCrJ **6**, 688 (2019).

[71] Y. Du, F. Tang, D. Wang, L. Sheng, E.-J. Kan, C.-G. Duan, S. Y. Savrasov, and X. Wan, Npj Quantum Mater. **2**, 3 (2017).

[72] H. Huang, J. Liu, D. Vanderbilt, and W. Duan, Phys. Rev. B **93**, 201114(R) (2016).

[73] X. M. Zhang, L. Jin, X. F. Dai, and G. D. Liu, J. Phys. Chem. Lett. **8**, 4814 (2017).

[74] J. L. Lu, W. Luo, X. Y. Li, S. Q. Yang, J. X. Cao, X. G. Gong, and H. J. Xiang, Chin. Phys. Lett. **34**, 057302 (2017).

[75] Y. Kim, B. J. Wieder, C. L. Kane, and A. M. Rappe, Phys. Rev. Lett. **115**, 036806 (2015).

[76] X. Zhang, B. Fu, L. Jin, X. Dai, G. Liu, and Y. Yao, J. Phys. Chem. C **123**, 25871 (2019).

[77] L. M. Schoop, M. N. Ali, C. Straßer, V. Duppel, S. S. P. Parkin, B. V. Lotsch, and C. R. Ast, Nat. Commun. **7**, 11696 (2016).

[78] F. Tran and P. Blaha, Phys. Rev. Lett. **102**, 226401 (2009).

[79] Q. Xu, R. Yu, Z. Fang, X. Dai, and H. Weng, Phys. Rev. B **95**, 045136 (2017).

[80] M. Zeng, C. Fang, G. Chang, Y.-A. Chen, T. Hsieh, A. Bansil, H. Lin, and L. Fu, arXiv:1504.03492.

[81] C. Xu, Y. Wang, R. Han, H. Tu, and Y. Yan, New J. Phys. **21**, 033005 (2019).

[82] Y. Xu, Y. Gu, T. Zhang, C. Fang, Z. Fang, X.-L. Sheng, and H. Weng, APL Mater. **7**, 101109 (2019).

[83] F. Zhou, Y. Liu, J. Wang, M. Kuang, T. Yang, H. Chen, X. Wang, and Z. Cheng, Phys. Rev. Mater. **5**, 074201 (2021).

[84] G. D. Liu, L. Jin, X. F. Dai, G. F. Chen, and X. M. Zhang, Phys. Rev. B **98**, 075157 (2018).

[85] S. Skaftouros, K. Özdoğan, E. Şaşıoğlu, and I. Galanakis, Phys. Rev. B **87**, 024420 (2013).

[86] S. V. Faleev, Y. Ferrante, J. Jeong, M. G. Samant, B. Jones, and S. S. P. Parkin, Phys. Rev. B **95**, 045140 (2017).

[87] M. E. Jamer, Y. J. Wang, G. M. Stephen, I. J. McDonald, A. J. Grutter, G. E. Sterbinsky, D. A. Arena, J. A. Borchers, B. J. Kirby, L. H. Lewis, B. Barbiellini, A. Bansil, and D. Heiman, Phys. Rev. Appl. **7**, 064036 (2017).

[88] S. Li, Z. M. Yu, Y. Liu, S. Guan, S. S. Wang, X. Zhang, Y. Yao, and S. A. Yang, Phys. Rev. B **96**, 081106(R) (2017).

[89] G. Chang, S.-Y. Xu, S.-M. Huang, D. S. Sanchez, C.-H. Hsu, G. Bian, Z.-M. Yu, I. Belopolski, N. Alidoust, H. Zheng, T.-R. Chang, H.-T. Jeng, S. A. Yang, T. Neupert, H. Lin, and M. Z. Hasan, Sci. Rep. **7**, 1688 (2017).

[90] X. Wang, F. Zhou, T. Yang, M. Kuang, Z. M. Yu, and G. Zhang, Phys. Rev. B **104**, L041104 (2021).

[91] R. Yu, Z. Fang, X. Dai, and H. Weng, Front. Phys. **12**, 127202 (2017).

[92] G.-B. Liu, M. Chu, Z. Zhang, Z.-M. Yu, and Y. Yao, Comput. Phys. Commun. **265**, 107993 (2021).

[93] F. Zhou, Z. Zhang, H. Chen, M. Kuang, T. Yang, and X. Wang, Phys. Rev. B **104**, 174108 (2021).

[94] Z.-M. Yu, W. K. Wu, X.-L. Sheng, Y. X. Zhao, and S. Y. A. Yang, Phys. Rev. B **99**, 121106(R) (2019).

[95] G. Liu, Y. J. Jin, Z. J. Chen, and H. Xu, Phys. Rev. B **104**, 024304 (2021).

[96] T. He, X. Zhang, Y. Liu, X. Dai, L. Wang, and G. Liu, Phys. Rev. B **104**, 045143 (2021).

[97] B. Feng, R.-W. Zhang, Y. Feng, B. Fu, S. Wu, K. Miyamoto, S. He, L. Chen, K. Wu, and K. Shimada *et al.*, Phys. Rev. Lett. **123**, 116401 (2019).

[98] R.-W. Zhang, Z. Zhang, C.-C. Liu, and Y. Yao, Phys. Rev. Lett. **124**, 016402 (2020).

[99] H. Zhang, X. Zhang, T. He, X. Dai, Y. Liu, G. Liu, L. Wang, and Y. Zhang, Phys. Rev. B **102**, 155116 (2020).

[100] H. Zhang, X. Zhang, Y. Liu, X. Dai, G. Chen, and G. Liu, Phys. Rev. B **102**, 195124 (2020).

[101] T. L. He, X. M. Zhang, T. Yang, Y. Liu, X. F. Dai, and G. D. Liu, Phys. Rev. Mater. **5**, 024205 (2021).

[102] P. V. Lukashev, Z. Lehmann, L. Stuelke, R. Filippone, B. Dahal, S. Valloppilly, J. Waybright, A. K. Pathak, Y. Huh, P. M. Shand, and P. Kharel, J. Alloys Compd. **895**, 162625 (2022).

[103] J. Goraus and J. Czerniewski, J. Magn. Magn. Mater. **498**, 166106 (2020).

[104] X. Wang, Z. Cheng, H. Yuan, and R. Khenata, J. Mater. Chem. C **5**, 11559 (2017).

[105] V. D. Esin, D. N. Borisenko, A. V. Timonina, N. N. Kolesnikov, and E. V. Deviatov, Phys. Rev. B **101**, 155309 (2020).

[106] W. Feng, X. Fu, C. Wan, Z. Yuan, X. Han, N. V. Quang, and S. Cho, Phys. Status Solidi RRL **9**, 641 (2015).